Time-Domain Method Having a Naturally Diagonal Mass Matrix Independent of Element Shape for General Electromagnetic Analysis—2-D Formulations

Jin Yan, *Student Member, IEEE*, and Dan Jiao, *Fellow, IEEE*

***Abstract*— In this paper, we present a new time-domain method that has a naturally diagonal mass matrix and thereby a strict linear computational complexity per time step, regardless of whether the discretization is a structured grid or an unstructured mesh. This property is obtained independent of the element shape used for discretization. No interpolations, projections, and mass lumping are required. The accuracy and stability of the proposed method are both theoretically guaranteed. In addition, no dual mesh is needed and the tangential continuity of the fields is satisfied across the element interface. The flexible framework of the proposed method also allows for a straightforward extension to higher order accuracy in both electric and magnetic fields. Numerical experiments have been conducted on a variety of unstructured triangular-element meshes. Correlations with analytical solutions and the time-domain finite-element method have validated the accuracy and generality of the proposed new time-domain method.**

***Index Terms*— Diagonal mass matrix, electromagnetic analysis, finite-difference time-domain (FDTD) methods, linear complexity, optimal complexity, time-domain finite-element methods (TDFEMs), time-domain methods, unstructured mesh.**

I. Introduction

IN TIME-DOMAIN methods for electromagnetic analysis, the finite-difference time-domain (FDTD) method [1], [2] has been a popular choice due to its simplicity and merit of being free of a system matrix solution. The computational complexity of the FDTD is linear (optimal) at each time step since the underlying mass matrix is diagonal, thus a matrix solution is avoided. The traditional FDTD method requires a structured grid. Its generalization to an unstructured mesh has been extensively studied. In [3]–[16] and many others, various schemes have been developed to extend the FDTD to deal with nonorthogonal grids and curved interfaces. They have significantly advanced the capability of the traditional FDTD method.

Manuscript received March 25, 2015; revised June 21, 2016; accepted January 3, 2017. Date of publication January 16, 2017; date of current version March 1, 2017. This work was supported in part by NSF under Award 1619062 and Award 1065318 and in part by DARPA under Award HR0011-14-1-0057.

The authors are with the School of Electrical and Computer Engineering, Purdue University, West Lafayette, IN 47907 USA (e-mail: djiao@purdue.edu).

Color versions of one or more of the figures in this paper are available online at http://ieeexplore.ieee.org.

Digital Object Identifier 10.1109/TAP.2017.2653078

Many of the non-orthogonal FDTD methods require a dual mesh that satisfies a certain relationship with the primary mesh. Such a dual mesh may not exist in a general unstructured mesh. For cases where the dual mesh exists, the accuracy of the resulting scheme can be low since between **E** and **H**, one of them cannot be centered by the integration loop of the other, and be perpendicular to the loop area. In the discrete surface integral-based methods [8], [12], local interpolation and projection techniques are developed to find the dual field from the primary field, and vice versa, which are shown to provide more accurate electric and magnetic fields. In addition to accuracy, the stability of the nonorthogonal FDTD methods has been studied. It is shown in [16] that as long as the discrete curl–curl operator supports complex-valued eigenvalues, an explicit scheme is unconditionally *unstable*. In theory, any real-valued but unsymmetrical matrix can have complex-valued eigenvalues that come in conjugate pairs. Therefore, once the discretized curl–curl operator is unsymmetric, the stability of the resultant explicit time marching cannot be guaranteed. However, the unsymmetric curl–curl operator is common in existing nonorthogonal FDTD methods, which is also often necessary in order to ensure the accuracy of these methods in an unstructured mesh. As a consequence, it remains a research problem how to ensure both accuracy and stability while preserving the matrix-free property of an FDTD-like method in an arbitrary unstructured mesh.

The finite-element method in time domain (TDFEM) [17] is capable of handling unstructured meshes. However, in both the first-order mixed **E**–**B** form [18] and [19] and the second-order vector wave equation based form [17], the TDFEM requires the solution of a mass matrix. The mass-lumping techniques enforce a matrix that is not diagonal in nature to be a diagonal one, which is error prone in an unstructured mesh [19]. Orthogonal vector basis functions have also been developed to render the mass matrix diagonal [20], [21]. Existing orthogonal vector bases are element-shape dependent, which further rely on an approximate integration to diagonalize the mass matrix. In addition, there exists a class of discontinuous Galerkin time-domain methods [22], [23], which only involves the solution of local matrices of a small size. However, this is achieved by *not* enforcing the tangential continuity of the fields across the element interface at the same time instant. Instead, the continuity is imposed through fluxes at previous time

steps. In contrast, both FDTD and TDFEM strictly impose the tangential continuity of the fields across the interfaces of discretization cells at the same time instant.

One observation that can be made on existing nonorthogonal Yee-like methods is that they all employ zeroth-order basis functions to represent the fields, in other words, both primary and dual fields are assumed to be constant along grid edges and tangential to the grid edges. Furthermore, both primary and dual fields are located on the surfaces of their respective mesh cells. Such a representation of the fields, though advantageous in preserving the divergence-free property of the fields locally, limits the accuracy of existing nonorthogonal methods especially in general unstructured meshes. To be specific, the **H** field is only second-order accurate at the center point of each **E**'s face and along the direction normal to **E**'s face. These points and directions are not coincident with the points and directions of the **H** located on the dual mesh. Hence, the desired **H** fields have to be obtained by interpolations and projections, which limits the accuracy and more critically, affects the stability. The same is true for the **E** field.

In this paper, we present a time-domain method that has a diagonal mass matrix in nature independent of the element shape used for discretization. In this method, given an arbitrary unstructured mesh, we use higher order vector bases to expand one field unknown in each element, whose curl is at least a linear function in space. As a result, we are able to obtain the other field unknown at any point along any direction *accurately* without a need for interpolation and projection. With this freedom, we can sample the other field unknown *across* the elements sharing the first field unknown in such a way that they can reversely produce the first field unknown accurately, without any need for interpolation and projection either. The resultant mass matrix is naturally diagonal, regardless of whether the discretization is structured or irregular. Its diagonal property is independent of the element shape, and its implementation is straightforward. The tangential continuity of the fields is also enforced across the element interface at each time instant. In addition, no dual mesh is needed in the proposed method. The flexible framework of the proposed method also allows for a straightforward extension to higher order accuracy in both **E** and **H**. Equally important, we have developed a new time-marching scheme to overcome the absolute instability caused by an unsymmetrical curl–curl operator, without sacrificing the optimal computational complexity resulting from the diagonal mass matrix, as well as the accuracy of the proposed method. Numerical simulations on various highly unstructured meshes have demonstrated the validity, accuracy, and stability of the proposed new method. Limited by space, only 2-D formulations and examples are presented in this paper. However, the essential idea of this paper is equally applicable to a 3-D analysis as can be seen from [24]–[27].

II. Proposed Framework

Consider a general electromagnetic problem discretized into *arbitrarily shaped* elements, which can also be a mix of different kinds of elements such as a mix of brick, triangular prism, and tetrahedral elements. Starting from the differential form of Faraday's law and Ampere's law

$$\nabla \times \mathbf{E} = -\mu \frac{\partial \mathbf{H}}{\partial t} \tag{1}$$

$$\nabla \times \mathbf{H} = \epsilon \frac{\partial \mathbf{E}}{\partial t} + \sigma \mathbf{E} + \mathbf{J} \tag{2}$$

we pursue a discretization of the above two equations, which results in a numerical system having a diagonal mass matrix in nature. Notice that the other two Maxwell's equations are implicitly satisfied by (1) and (2).

To discretize Faraday's law (1), we expand the electric field **E** in each element by certain vector basis functions $\mathbf{N}_i$ $(i = 1, 2, \ldots, m)$ as follows:

$$\mathbf{E} = \sum_{j=1}^{m} e_j \mathbf{N}_j \tag{3}$$

where e_j is the unknown coefficient of the jth vector basis. Using (1) and (3), we can obtain magnetic field **H** at any point. Assume that we compute **H** at N_h discrete points, each of which is denoted by $\mathbf{r}_{hi}, i = 1, 2, \ldots, N_h$. At each **H**-point, assume the unit vector along which we compute **H** is $\hat{h}_i$. Substituting (3) into (1), evaluating **H** at the N_h points, and taking the dot product of the resultant with corresponding $\hat{h}_i$ at each point, we obtain the following N_h equations:

$$\hat{h}_i \cdot \sum e_j \{\nabla \times \mathbf{N}_j\}(\mathbf{r}_{hi}) = -\hat{h}_i \cdot \mu(\mathbf{r}_{hi}) \frac{\partial \mathbf{H}(\mathbf{r}_{hi})}{\partial t} \quad (i = 1, 2, \ldots, N_h) \tag{4}$$

which can further be compactly written as the following matrix equation:

$$\mathbf{S}_e\{e\} = -\text{diag}(\{\mu\}) \frac{\partial \{h\}}{\partial t} \tag{5}$$

where $\{e\}$ is a global vector containing the unknown coefficients e_i of **E**'s vector bases, and $\{h\}$ is a global vector containing discretized **H**. Their ith entries are

$$e_i = \mathbf{E}(\mathbf{r}_{ei}) \cdot \hat{e}_i \tag{6}$$

$$h_i = \mathbf{H}(\mathbf{r}_{hi}) \cdot \hat{h}_i \tag{7}$$

in which $\mathbf{r}_{ei}$ and $\hat{e}_i$ $(i = 1, 2, \ldots, N_e)$ are, respectively, the points and the unit-vectors associated with the vector **E**'s degrees of freedom. In (5), $\text{diag}(\{\mu\})$ is a diagonal matrix of size N_h, whose ith diagonal entry is the permeability at point $\mathbf{r}_{hi}$. The sparse matrix $\mathbf{S}_e$ is rectangular of dimension N_h by N_e, the length of $\{e\}$ is N_e; while that of $\{h\}$ is N_h.

To discretize Ampere's law (2), we evaluate **E** at the $\mathbf{r}_{ei}$ $(i = 1, 2, \ldots, N_e)$ points, and take the dot product of the resultant with $\hat{e}_i$ at each point, obtaining

$$\hat{e}_i \cdot \{\nabla \times \mathbf{H}\}(\mathbf{r}_{ei}) = \epsilon(\mathbf{r}_{ei}) \frac{\partial e_i}{\partial t} + \sigma(\mathbf{r}_{ei}) e_i + \hat{e}_i \cdot \mathbf{J}(\mathbf{r}_{ei}) \quad (i = 1, 2, \ldots, N_e) \tag{8}$$

where $\hat{e}_i \cdot \nabla \times \mathbf{H}$ is generated by using $\{h\}$ obtained from (5). As a result, we obtain the following discretization of Ampere's law:

$$\mathbf{S}_h\{h\} = \text{diag}(\{\epsilon\}) \frac{\partial \{e\}}{\partial t} + \text{diag}(\{\sigma\})\{e\} + \{j\} \tag{9}$$

where the sparse matrix $\mathbf{S}_h$ is of dimension $N_e \times N_h$, and the ith entry of current source vector $\{j\}$ in (9) is

$$j_i = \hat{e}_i \cdot \mathbf{J}(\mathbf{r}_{ei}), \quad (i = 1, 2, \ldots, N_e). \tag{10}$$

In addition, diag($\{\epsilon\}$) and diag($\{\sigma\}$) are diagonal, whose ith entry is, respectively, the permittivity and conductivity at point $\mathbf{r}_{ei}$.

A leap-frog-based time discretization of (5) and (9) clearly provides us with a time-marching scheme free of matrix solutions as follows:

$$\{h\}^{n+\frac{1}{2}} = \{h\}^{n-\frac{1}{2}} - \text{diag}\left(\left\{\frac{1}{\mu}\right\}\right) \Delta t \mathbf{S}_e \{e\}^n \tag{11}$$

$$\left(\text{diag}(\{\epsilon\}) + \frac{\Delta t}{2}\text{diag}(\{\sigma\})\right)$$

$$\{e\}^{n+1} = \left(\text{diag}(\{\epsilon\}) - \frac{\Delta t}{2}\text{diag}(\{\sigma\})\right)\{e\}^n + \Delta t \mathbf{S}_h \{h\}^{n+\frac{1}{2}} - \Delta t \{j\}^n \tag{12}$$

where Δt is the time step, and the time instants for $\{e\}$ and $\{h\}$, denoted by superscripts, are staggered by half. Note that neither (11) nor (12) involves a matrix solution.

Equations (5) and (9) can also be solved in a second-order fashion. Taking another time derivative of (9) and substituting (5), we obtain

$$\frac{\partial^2 \{e\}}{\partial t^2} + \text{diag}\left(\left\{\frac{\sigma}{\epsilon}\right\}\right)\frac{\partial \{e\}}{\partial t} + \mathbf{S}\{e\} = -\text{diag}\left(\left\{\frac{1}{\epsilon}\right\}\right)\frac{\partial \{j\}}{\partial t} \tag{13}$$

where

$$\mathbf{S} = \text{diag}\left(\left\{\frac{1}{\epsilon}\right\}\right)\mathbf{S}_h \text{diag}\left(\left\{\frac{1}{\mu}\right\}\right)\mathbf{S}_e. \tag{14}$$

It is obvious that the above numerical system is also free of matrix solutions with a central-difference-based discretization in time. In fact, it can be readily proved that (11) and (12) are the same as the central-difference-based discretization of second-order system (13) after eliminating the $\{h\}$-unknown. In addition, the mass matrix shown in (13), which is the matrix in front of the second-order time derivative, is obviously diagonal. Hence, no mass lumping is needed. For anisotropic materials whose permittivity and permeability are tensors, the diagonal mass matrix simply becomes a block diagonal matrix whose block size is 3. Hence, its inverse is also explicit, which can be found analytically.

III. Proposed Formulations

A. General Idea

At this point, it can be seen that the accuracy of the proposed method relies on an accurate construction of (9) for an arbitrary unstructured mesh, since the accuracy of (5) is not a concern at all—with a set of well-established curl-conforming vector basis functions for discretizing **E**, the accuracy of (5) is guaranteed for producing **H** at any point and along any direction. Therefore, the key issue is how to build an accurate (9). To be more precise, how to construct $\mathbf{S}_h\{h\}$, i.e., a discretization of the curl of **H**, such that it can accurately produce the desired $\{e\}$.

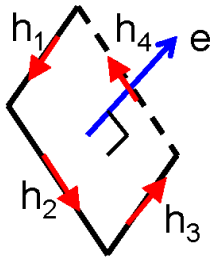

Fig. 1. **H** points and directions determined based on **E**'s degrees of freedom.

We propose to determine **H** points and directions based on discretized **E** unknowns so that the resultant **H** fields can generate the desired $\{e\}$ accurately. From the integral form of Ampere's law, we know that the circulation of the tangential **H** in a loop can produce an accurate **E** along the direction *normal* to the loop at the *center* point of the loop area. Hence, the simplest approach is for each $\hat{e}_i$ located at point $\mathbf{r}_{ei}$, define a rectangular loop perpendicular to $\hat{e}_i$ and centered at point $\mathbf{r}_{ei}$, as illustrated in Fig. 1. Along this loop, we define **H**-points and **H**-directions associated with $\hat{e}_i$. The set of **H**-points and **H**-directions found for each $\hat{e}_i$ at $\mathbf{r}_{ei}$ makes the whole set of **H**-points denoted by $\{\mathbf{r}_{hi}\}$, and the whole set of **H**-directions denoted by $\{\hat{h}_i\}$, with $(i = 1, 2, \ldots, N_h)$. The $\{h\}$ is simply the vector of $\mathbf{H}(\mathbf{r}_{hi}) \cdot \hat{h}_i$ $(i = 1, 2, \ldots, N_h)$ as shown in (7). With such an $\{h\}$, the $\mathbf{S}_h$ can be readily built with guaranteed accuracy. In addition, no dual mesh needs to be constructed for discretizing **H** since the **H** is known from (5) at any point and along any direction. We only need to sample **H** at the points along the directions shown in Fig. 1 based on **E**'s points and directions. In fact, our discrete **H** does not form a mesh at all.

B. Vector Basis Functions for the Expansion of E

Consider an arbitrary ith edge in a triangular mesh residing on an xy plane, as the one labeled by e in Fig. 2(a). Using the normalized zeroth-order edge elements to expand **E**, the e_i shown in (6) has $\hat{e}_i$ the unit vector tangential to the ith edge, and $\mathbf{r}_{ei}$ the center point of the ith edge. To obtain such an e_i accurately from the discrete **H** (now H_z only for a 2-D TE case), the two **H**-points should be located on the line that is perpendicular to the ith edge and centered at the point $\mathbf{r}_{ei}$, as illustrated in Fig. 2(a). In this way, the edge is perpendicular to the **H**-loop (in the plane defined by z-direction and the line normal to the edge), and resides at the center of the loop. As a result, an accurate $\mathbf{E} \cdot \hat{e}_i$ can be obtained. However, using the zeroth-order edge elements, the curl of **E** is constant in every element, thus we cannot generate **H** at the desired points accurately. From another point of view, we can view the **H** obtained at the center point of every element to be second-order accurate, but not at other points. However, in an arbitrary unstructured mesh, the line segment connecting the center points of the two elements sharing an edge may not be perpendicular to the edge, and the two center points may not have the same distance to the edge either, as illustrated in Fig. 2(b).

To overcome the aforementioned problem, we propose to use a higher order curl-conforming vector basis to expand **E**

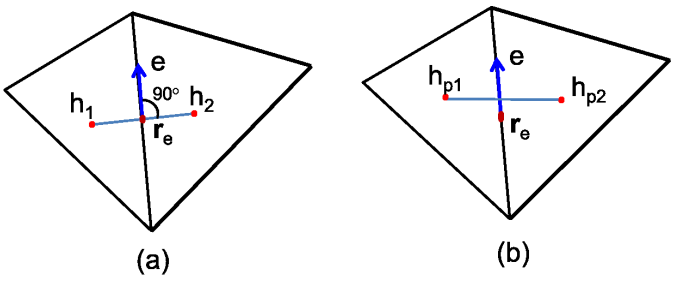

Fig. 2. (a) Locations of **H** points required for the accurate evaluation of e at point $\mathbf{r}_e$. (b) Locations of **H** points with zeroth-order edge bases.

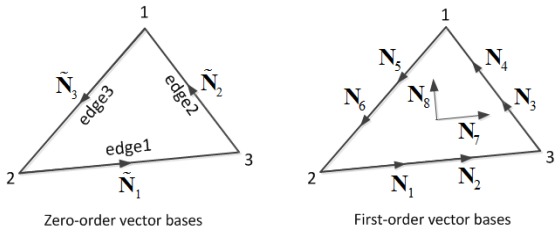

Fig. 3. Illustration of the degrees of freedom of the zeroth- and the first-order vector bases in a triangular element.

in each element. With an order higher than zero, the curl of **E** and hence **H** is at least a linear function in each element. In this way, we can generate **H** at any desired point accurately from (5).

However, we cannot blindly use the original set of the first-order curl-conforming vector bases in [28]. They need certain modifications to fit the need of this paper. This is because the unknown coefficient e_i shown in (3) should be equal to (6) to connect (5) with (9) directly without any need for transformation (if conventional first-order bases are used, the proposed method equally produces a diagonal mass matrix by using an unknown transformation [25], [26]). This results in the following property of the desired vector basis functions:

$$\begin{aligned} \hat{e}_i \cdot \mathbf{N}_j(\mathbf{r}_{ei}) &= 1, \quad j = i \\ \hat{e}_i \cdot \mathbf{N}_j(\mathbf{r}_{ei}) &= 0, \quad j \neq i \end{aligned} \tag{15}$$

which can be readily obtained by taking a dot product with $\hat{e}_i$ on both sides of (3) at point $\mathbf{r}_{ei}$, and recognizing that the left-hand side of the resultant is required to be equal to e_i. Notice that (15) is not mass lumping that enforces the volume/area integral of $\mathbf{N}_i \cdot \mathbf{N}_j$ to be δ_{ij}. The zeroth-order edge bases in a triangular or other shaped elements naturally satisfy (15). As for the first-order edge basis functions, there are not only six edge degrees of freedom, but also two internal degrees of freedom at the center point of a triangular element. The former six bases satisfy (15), but the latter two do not. They hence need a modification. The definitions of these two bases are not unique either, thus they can be modified to satisfy (15) without sacrificing the completeness of the bases.

To elaborate, first, we list the original six edge vector basis functions $\mathbf{N}_i$ $(i = 1, 2, \ldots, 6)$ together with their unit tangential vectors $\hat{e}_i$ as follows:

$$\begin{aligned} \hat{e}_1 &= \vec{v}_{23}/\|\vec{v}_{23}\|, \quad \mathbf{N}_1 = (3\xi_2 - 1)\mathbf{W}_1 \\ \hat{e}_2 &= \vec{v}_{23}/\|\vec{v}_{23}\|, \quad \mathbf{N}_2 = (3\xi_3 - 1)\mathbf{W}_1 \\ \hat{e}_3 &= \vec{v}_{31}/\|\vec{v}_{31}\|, \quad \mathbf{N}_3 = (3\xi_3 - 1)\mathbf{W}_2 \\ \hat{e}_4 &= \vec{v}_{31}/\|\vec{v}_{31}\|, \quad \mathbf{N}_4 = (3\xi_1 - 1)\mathbf{W}_2 \\ \hat{e}_5 &= \vec{v}_{12}/\|\vec{v}_{12}\|, \quad \mathbf{N}_5 = (3\xi_1 - 1)\mathbf{W}_3 \\ \hat{e}_6 &= \vec{v}_{12}/\|\vec{v}_{12}\|, \quad \mathbf{N}_6 = (3\xi_2 - 1)\mathbf{W}_3 \end{aligned} \tag{16}$$

where $\vec{v}_{ij}$ denotes the vector pointing from node i to node j, as shown in Fig. 3, ξ_i $(i = 1, 2, 3)$ are area coordinates, and **W** denotes the normalized zeroth-order edge basis as follows:

$$\begin{aligned} \mathbf{W}_1 &= L_1(\xi_2 \nabla\xi_3 - \xi_3 \nabla\xi_2) \\ \mathbf{W}_2 &= L_2(\xi_3 \nabla\xi_1 - \xi_1 \nabla\xi_3) \\ \mathbf{W}_3 &= L_3(\xi_1 \nabla\xi_2 - \xi_2 \nabla\xi_1) \end{aligned} \tag{17}$$

in which L_i is the length of the ith edge. The degrees of freedom of the above six edge vector bases are located, respectively, at the following points in each element:

$$\begin{aligned} \mathbf{r}_{e1} &= (\xi_2 = 2/3, \xi_3 = 1/3) \\ \mathbf{r}_{e2} &= (\xi_2 = 1/3, \xi_3 = 2/3) \\ \mathbf{r}_{e3} &= (\xi_1 = 1/3, \xi_3 = 2/3) \\ \mathbf{r}_{e4} &= (\xi_1 = 2/3, \xi_3 = 1/3) \\ \mathbf{r}_{e5} &= (\xi_1 = 2/3, \xi_2 = 1/3) \\ \mathbf{r}_{e6} &= (\xi_1 = 1/3, \xi_2 = 2/3). \end{aligned} \tag{18}$$

The projection of $\hat{e}_i$ $(i = 1, 2, \ldots, 6)$ onto any jth vector basis in (16) at the point of the ith degree of freedom, i.e., $\hat{e}_i \cdot \mathbf{N}_j(\mathbf{r}_{ei})$, is obviously zero for $j \neq i$ and 1 for $j = i$. This can be analytically verified, and also conceptually understood because if it is not zero, the first-order bases (16) cannot ensure the tangential continuity of **E** across the element interfaces, which is not true. Therefore, the property of (15) is satisfied for $(i = 1, 2, \ldots, 6)$ and $(j = 1, 2, \ldots, 6)$.

For the two vector basis functions whose degrees of freedom are internal at the element center, we have

$$\begin{aligned} \mathbf{r}_{e7} &= (\xi_1 = 1/3, \xi_2 = 1/3) \\ \mathbf{r}_{e8} &= (\xi_1 = 1/3, \xi_2 = 1/3). \end{aligned} \tag{19}$$

If we choose the two vector bases as $\mathbf{N}_7 = (9/2)\xi_1\mathbf{W}_1$ and $\mathbf{N}_8 = (9/2)\xi_2\mathbf{W}_2$ as those suggested in [28], with $\hat{e}_7 = \vec{v}_{23}/\|\vec{v}_{23}\|$ along edge 1, and $\hat{e}_8 = \vec{v}_{31}/\|\vec{v}_{31}\|$ along edge 2, although they make $\hat{e}_i \cdot \mathbf{N}_j(\mathbf{r}_{ei})$ zero for $(i = 1, 2, \ldots, 6)$ and $(j = 7, 8)$, the $\hat{e}_7 \cdot \mathbf{N}_8(\mathbf{r}_{e7})$ is, in general, not zero since edge 1 may not be perpendicular to $\mathbf{W}_2$ at the element center. Thus, (15) is not satisfied. If we keep $\mathbf{N}_7$ as it is, but choosing $\mathbf{N}_8$ as $\xi_2\xi_3\nabla\xi_1$, although $\hat{e}_7 \cdot \mathbf{N}_8(\mathbf{r}_{e7})$ becomes zero now, $\hat{e}_8 \cdot \mathbf{N}_7(\mathbf{r}_{e8})$ is not zero in general at the element center. Even though we change $\hat{e}_8$ to be along the direction of $\nabla\xi_1$, $\hat{e}_8 \cdot \mathbf{N}_7(\mathbf{r}_{e8})$ is not zero either since $\mathbf{W}_1$ is not parallel to edge 1 at element center. In view of the aforementioned problem, we propose to keep one basis ($\mathbf{N}_7$) the same as before, but modify the second

basis ($\mathbf{N}_8$) as follows:

$$\hat{e}_7 = \vec{v}_{23}/\|\vec{v}_{23}\|, \quad \mathbf{N}_7 = \frac{9}{2}\xi_1\mathbf{W}_1$$
$$\hat{e}_8 = (\hat{z}\times\mathbf{W}_1)/\|\hat{z}\times\mathbf{W}_1\|, \quad \mathbf{N}_8 = c_8\xi_2\xi_3\nabla\xi_1 \tag{20}$$

where c_8 is the normalization coefficient that makes $\hat{e}_8 \cdot \mathbf{N}_8(\mathbf{r}_{e8}) = 1$. In (20), instead of using the $\nabla\xi_1$ direction as $\hat{e}_8$, we employ the direction of $(\hat{z}\times\mathbf{W}_1)$. By doing so, $\hat{e}_8\cdot\mathbf{N}_7(\mathbf{r}_{e8})$ is ensured to be zero. Furthermore, $\hat{e}_7 \cdot \mathbf{N}_8(\mathbf{r}_{e7}) = 0$ still holds true. In addition, with the choice of (20), the property of $\hat{e}_i \cdot \mathbf{N}_j(\mathbf{r}_{ei}) = 0$ with $(i = 1, 2, \ldots, 6)$ and $(j = 7, 8)$ is still satisfied. Meanwhile, the property of $\hat{e}_i \cdot \mathbf{N}_j(\mathbf{r}_{ei}) = 0$ with $(i = 7, 8)$ and $(j = 1, 2, \ldots, 6)$ is also satisfied since all the six edge vector bases vanish at the element center.

In summary, the six vector basis functions shown in (16) and the two vector bases given by (20) make a complete set of the first-order vector basis functions for a triangular element. Together with the unit vectors $\hat{e}_i$ defined in (16) and (20), they meet the requirements of (15), and hence making each entry in $\{e\}$ nothing but $\mathbf{E}\cdot\hat{e}_i(\mathbf{r}_{ei})$. It is also worth mentioning that the approach shown in (20) for modifying bases is equally applicable to other higher order bases to make the unknown coefficient vector of the basis functions equal to the unknown electric field vector shown in (6).

C. Choice of H-Points and H-Directions

With the points and directions of the **E**'s degrees of freedom known from the above section, it also becomes clear at which points and along which directions we evaluate **H**. As shown in Fig. 2(a), for each $\hat{e}_i$ located at $\mathbf{r}_{ei}$, we draw a line perpendicular to $\hat{e}_i$ at $\mathbf{r}_{ei}$. On this line, we find two points such that the center point of the two points is $\mathbf{r}_{ei}$. The two points are where we need to prepare for **H** such that $\mathbf{E}\cdot\hat{e}_i$ can be accurately evaluated at $\mathbf{r}_{ei}$. For $\hat{e}_i$ located at the edge, the two points straddle the edge, and reside, respectively, in the two elements sharing the edge; for the internal degree of freedom whose $\hat{e}_i$ is located at the element center, both **H**-points are chosen inside the element. The union of the two points we find for each $\hat{e}_i$ makes the whole set of $\mathbf{r}_{hi}$ $(i = 1, 2, \ldots, N_h)$. As for the direction used at each **H**-point, for analyzing 2-D problems, it is $\hat{h}_i = \hat{z}$ $(i = 1, 2, \ldots, N_h)$.

Fig. 4 illustrates the locations of the **H**-points drawn for the **E** unknowns located in a single element. Basically, each **E** unknown is associated with a pair of **H**-points. Each pair is marked by a different color in Fig. 4. Coincident H-field points are permitted in the proposed algorithm. No extra checking to avoid overlapping points is needed.

The total number of **E** unknowns, i.e., the length of $\{e\}$ vector in (5), is $N_e = 2N_{\text{edge}} + 2N_{\text{patch}}$; whereas the total number of **H** unknowns, i.e., the length of $\{h\}$ vector, is $N_h = 10N_{\text{patch}}$ since there are 10 **H**-points in each patch.

D. Formulations of $\mathbf{S}_e$ and $\mathbf{S}_h$

$\mathbf{S}_e$ is a sparse matrix of size $N_h \times N_e$, whose ijth entry can be written as

$$\mathbf{S}_{e,ij} = \hat{h}_i \cdot \{\nabla\times\mathbf{N}_j\}(\mathbf{r}_{hi}) \tag{21}$$

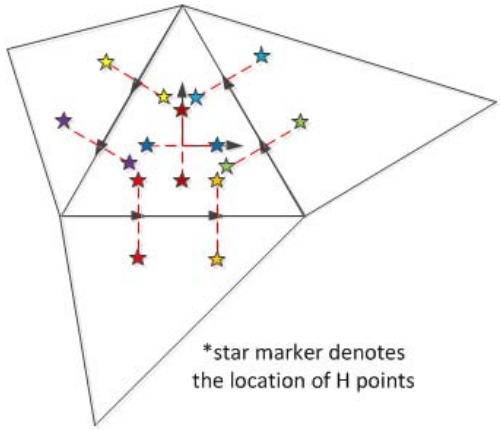

Fig. 4. Illustration of **H**-points (stars) for all **E**'s degrees of freedom (arrows) in one element.

where i denotes the global index of the **H**-point, while j is the global index of the **E**'s vector basis function. The number of nonzero elements in each row of $\mathbf{S}_e$ is 8 since the H_z at each specified point is evaluated from the curl of **E** expanded into eight vector basis functions in the element where the **H**-point resides. When $\mathbf{S}_e$ is constructed, the elements share the same tangential **E**, i.e., $\{e\}$, in common along the edges, thus the tangential continuity of **E** is enforced during the construction of $\mathbf{S}_e$. The curl of each vector basis $\mathbf{N}_j$ in (21) can be evaluated analytically based on their expressions given in (16) and (20), and then the point $\mathbf{r}_{hi}$ is substituted into the resulting analytical expression to obtain the curl at the point.

The size of $\mathbf{S}_h$ is still the same as that of the transpose of $\mathbf{S}_e$, namely, $N_e \times N_h$. However, it is not the transpose of $\mathbf{S}_e$. Consider an arbitrary **E**-unknown e_i, and denote the two **H**-unknowns associated with it to be h_m, and h_n, respectively. Assume the distance between h_m and h_n is l_i. Since the two **H**-points of each e_i are positioned in a way as that shown in Fig. 4, the discretization of $\nabla\times\mathbf{H}$ for e_i becomes $\pm(h_m - h_n)/l_i$. Therefore, every row of $\mathbf{S}_h$ has only two nonzero elements, whose entries are

$$\mathbf{S}_{h,ij} = \pm\frac{1}{l_i} \tag{22}$$

where j denotes the global index of the **H**-point associated with the e_i.

E. Time Marching Scheme and Stability Analysis

For a general unstructured mesh, if we choose $\mathbf{S}_h = \mathbf{S}_e^T$, the accuracy cannot be ensured. For an accurate $\mathbf{S}_h$ constructed in the proposed work, it is not the transpose of $\mathbf{S}_e$. The resultant **S** is not symmetric. As a result, the explicit marching like (11) and (12) or a central-difference-based explicit time marching of (13) is absolutely unstable.

To understand the stability problem more clearly, we can perform a stability analysis of the central-difference-based time discretization of (13) based on the approach given in [16] and [29]. We start with a general inhomogeneous lossless problem since the analysis of a lossy problem can be done in a similar way. The z-transform of the central-difference-based

time marching of (13) results in the following equation:

$$(z-1)^2 + \Delta t^2 \lambda z = 0 \tag{23}$$

where λ is the eigenvalue of $\mathbf{S}$. The two roots of (23) can be readily found as

$$z_{1,2} = \frac{2 - \Delta t^2 \lambda \pm \sqrt{\Delta t^2 \lambda (\Delta t^2 \lambda - 4)}}{2}. \tag{24}$$

If $\mathbf{S}$ is Hermitian positive semidefinite, its λ is real and no less than zero. Thus, we can always find a time step to make z in (24) bounded by 1, and hence the explicit simulation of (13) stable. Such a time step satisfies $\Delta t \leq 2/\sqrt{\lambda_{\max}}$, where λ_{max} is the maximum eigenvalue, which is also $\mathbf{S}$'s spectral radius. However, if $\mathbf{S}$ is not Hermitian positive semidefinite, its eigenvalues either are real or come in complex-conjugate pairs [30]. For complex-valued or negative eigenvalues λ, the two roots z_1 and z_2 shown in (24) satisfy $z_1 z_2 = 1$ and neither of them has modulus equal to 1. As a result, the modulus of one of them must be greater than 1, and hence the explicit time-domain simulation of (13) must be unstable. Similarly, we can perform a stability analysis of a general lossy problem, and find the same conclusion—if $\mathbf{S}$ is not symmetric and supports complex-valued and/or negative eigenvalues, the central-difference-based explicit timed-domain simulation of (13) is absolutely unstable.

The stability problem is solved in this paper by developing a time marching scheme that is stable and requires no matrix inversion. We will start with the following backward-difference-based discretization of (13) to explain the basic idea. But the final time marching equation only involves the field solutions at previous time steps for obtaining the field solution at current time step. The backward-difference-based discretization of (13) results in

$$\begin{aligned}&\{e\}^{n+1} - 2\{e\}^n + \{e\}^{n-1} \\ &\quad + \Delta t \mathrm{diag}\left(\left\{\frac{\sigma}{\epsilon}\right\}\right)(\{e\}^{n+1} - \{e\}^n) + \Delta t^2 \mathbf{S}\{e\}^{n+1} \\ &\quad = -\Delta t^2 \mathrm{diag}\left(\left\{\frac{1}{\epsilon}\right\}\right)\left(\frac{\partial\{j\}}{\partial t}\right)^{n+1}\end{aligned} \tag{25}$$

which is obtained by approximating both first- and second-order time derivatives by a backward-difference scheme [17]. Performing a stability analysis of (25), we find the two roots of z as

$$z_{1,2} = \frac{1}{1 \pm j\Delta t\sqrt{\lambda}}. \tag{26}$$

As a result, z can still be bounded by 1 even for an infinitely large time step. However, this does not mean the backward difference is unconditionally stable since now the λ can be complex-valued or even negative. To make the magnitude of (26) bounded by 1, we find that the time step needs to satisfy the following condition:

$$\Delta t > 2\frac{|\mathrm{Im}(\sqrt{\lambda})|}{|\sqrt{\lambda}|^2} \tag{27}$$

where $\mathrm{Im}(\cdot)$ denotes the imaginary part of $(\cdot)$. Interestingly, the scheme is stable for large time step, but not stable for small time step. For real eigenvalues, it is absolutely stable. However, for complex or negative eigenvalues, to be stable, one should not choose a small time step that violates (27).

Rearranging the terms in (25), we obtain

$$\begin{aligned}\tilde{\mathbf{D}}\{e\}^{n+1} &= 2\{e\}^n - \{e\}^{n-1} + \Delta t \mathrm{diag}\left(\left\{\frac{\sigma}{\epsilon}\right\}\right)\{e\}^n \\ &\quad - \Delta t^2 \mathrm{diag}\left(\left\{\frac{1}{\epsilon}\right\}\right)\left(\frac{\partial\{j\}}{\partial t}\right)^{n+1}\end{aligned} \tag{28}$$

where

$$\tilde{\mathbf{D}} = \mathbf{I} + \Delta t \mathrm{diag}\left(\left\{\frac{\sigma}{\epsilon}\right\}\right) + \Delta t^2 \mathbf{S}. \tag{29}$$

Let the diagonal part of $\tilde{\mathbf{D}}$ be $\mathbf{D}$, thus

$$\mathbf{D} = \mathbf{I} + \Delta t \mathrm{diag}\left(\left\{\frac{\sigma}{\epsilon}\right\}\right). \tag{30}$$

Front multiplying both sides of (28) by $\mathbf{D}^{-1}$, we obtain

$$(\mathbf{I} + \tilde{\mathbf{M}})\{e\}^{n+1} = \mathbf{D}^{-1}\{f\} \tag{31}$$

where $\{f\}$ is the right-hand side of (28), and

$$\tilde{\mathbf{M}} = \Delta t^2 \mathbf{D}^{-1}\mathbf{S}. \tag{32}$$

Although (28) permits the use of any large time step, we choose the time step in the following way:

$$\Delta t^2 < \frac{1}{\|\mathbf{S}\|} \tag{33}$$

and hence

$$\Delta t^2 \|\mathbf{S}\| < 1 \tag{34}$$

where $\|\mathbf{S}\|$ denotes the norm of $\mathbf{S}$. Notice that the time step determined from (33) is the same as that of a traditional explicit scheme for stability. This is also the time step required by accuracy when space step is determined based on the input spectrum. This is because the square root of spectral radius and thereby the norm of $\mathbf{S}$ corresponds to the largest frequency present in the system response. To capture this frequency accurately, a time step of (33) is necessary. It is also worth mentioning that the time step that violates (27) turns out to be very small in the proposed method since the imaginary part of the complex eigenvalues is generally negligible compared to the real part. Thus, (33) satisfies (27) in general.

The $\mathbf{D}$ is a diagonal matrix shown in (30). The norm of its inverse can be analytically evaluated as

$$\|\mathbf{D}^{-1}\| = 1/\min_{1 \leq i \leq N_e}(1 + \Delta t \sigma_i/\epsilon_i) = 1 \tag{35}$$

we hence obtain, from (34) and (35)

$$\|\tilde{\mathbf{M}}\| = \Delta t^2 \|\mathbf{D}^{-1}\mathbf{S}\| \leq \Delta t^2 \|\mathbf{D}^{-1}\| \|\mathbf{S}\| < 1. \tag{36}$$

As a result, we can evaluate the inverse of $\mathbf{I} + \tilde{\mathbf{M}}$ by

$$(\mathbf{I} + \tilde{\mathbf{M}})^{-1} = \mathbf{I} - \tilde{\mathbf{M}} + \tilde{\mathbf{M}}^2 - \tilde{\mathbf{M}}^3 + \cdots \tag{37}$$

which can be truncated since (36) is satisfied. Together with the fact that the mass matrix $\mathbf{D}$ is diagonal, and thus $\tilde{\mathbf{M}}$ does not involve any matrix inversion, the system matrix has an explicit inverse, and hence no matrix solutions are required in the proposed method. This is very different from an iterative

matrix solution that does not have an explicit inverse of the system matrix. Equation (31) can then be computed as

$$\{e\}^{n+1} = (\mathbf{I} - \tilde{\mathbf{M}} + \tilde{\mathbf{M}}^2 - \cdots + (-\tilde{\mathbf{M}})^k)\mathbf{D}_i\{f\} \qquad (38)$$

where $\mathbf{D}_i$ is diagonal matrix $\mathbf{D}$'s inverse. The number of terms k is ensured to be small (less than 10) since (36) holds true. When mesh changes, the spectral radius of $\mathbf{S}$ changes. However, the time step required by accuracy or by a traditional explicit scheme for stability also changes. Since such a time step is chosen based on the criterion of (33), the convergence of (37) is guaranteed and the convergence rate does not depend on the mesh quality.

The computational cost of (38) is k sparse matrix-vector multiplications since each term can be computed from the previous term. For example, after $\mathbf{D}_i\{f\}$ is computed, let the resultant be vector y, the second term in (38) can be obtained from $-\tilde{\mathbf{M}}y$. Let the resultant be y. The third term relating to $\tilde{\mathbf{M}}^2$ is nothing but $\tilde{\mathbf{M}}y$. Therefore, the cost for computing each term in (38) is the cost of multiplying $\tilde{\mathbf{M}}$ by the vector obtained at the previous step, thus the overall computational complexity is strictly linear (optimal).

When the proposed method is applied to a regular orthogonal grid, we do not need to add a few more sparse matrix-vector multiplications shown in (38). One sparse matrix-vector multiplication based on $\tilde{\mathbf{M}}$ is sufficient for stability. Only for unstructured meshes where complex-valued or negative eigenvalues exist, (38) is necessary for stability. The key for (38) to be free of matrix inversion is the diagonal mass matrix created by the proposed new method for discretizing Maxwell's equations in unstructured meshes. The same series expansion can be applied to the backward-difference-based TDFEM, but the resultant scheme still involves a matrix solution.

F. Imposing Boundary Conditions

The implementation of boundary conditions in the proposed method is similar to that in the TDFEM and FDTD, since the proposed method has a numerical system conformal to the two methods.

For closed-region problems, the perfect electric conductor (PEC), the perfect magnetic conductor (PMC), or other nonzero prescribed tangential $\mathbf{E}$ or tangential $\mathbf{H}$ are commonly used at the boundary. To impose prescribed tangential $\mathbf{E}$ at N_b boundary points, in (5), we simply set the $\{e\}$ entries at the N_b points to be the prescribed value, and keep the size of $\mathbf{S}_e$ the same as before to produce all N_h discrete $\mathbf{H}$ from the N_e discrete $\mathbf{E}$. In (9), since the $\{e\}$ entries at the N_b points are known, the updating of (9) only needs to be performed for the rest $(N_e - N_b)$ $\{e\}$ entries. As a result, we can remove the N_b rows from $\mathbf{S}_h$ corresponding to the N_b boundary $\mathbf{E}$ fields, while keeping the column dimension of $\mathbf{S}_h$ the same as before. The above treatment, from the perspective of the second-order system shown in (13), is the same as keeping just $(N_e - N_b)$ rows of $\mathbf{S}$, providing the full-length $\{e\}$ (with the boundary entries specified) for the $\{e\}$ multiplied by $\mathbf{S}$, but taking only the $N_e - N_b$ rows of all the other terms involved in (13). To impose a PMC

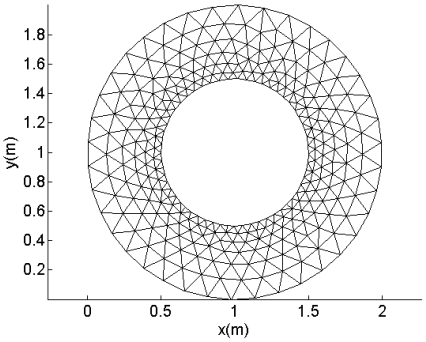

Fig. 5. Illustration of the mesh of a ring structure.

to truncate the computational domain, the total $\mathbf{E}$ unknown number is N_e without any reduction. The (5) is formulated as it is since the $\mathbf{H}$-points having the PMC boundary condition can be placed outside the computational domain, instead of right on the boundary where $\mathbf{E}$ is located. As for (9), there is no need to make any change either since the tangential $\mathbf{H}$ is set to be zero outside the computational domain. For open-region problems, the framework of (5) and (9) in the proposed method is conformal to that of the FDTD. As a result, the various absorbing boundary conditions that have been implemented in FDTD such as the commonly used perfectly matched layer (PML) can be implemented in the same way in the proposed method.

IV. Numerical Results

In this section, we simulate a variety of 2-D unstructured meshes to demonstrate the validity and generality of the proposed method in analyzing arbitrarily shaped structures discretized into irregular mesh elements. The accuracy of the proposed method is validated by comparison with both analytical solutions and the TDFEM method that is capable of handling unstructured meshes but having a mass matrix that is not diagonal.

A. Wave Propagation in a 2-D Ring Mesh

A 2-D ring centered at (1.0 m, 1.0 m) with inner radius 0.5 m and outer radius 1.0 m is simulated in free space. The triangular mesh is generated by DistMesh [31], the details of which are shown in Fig. 5. The discretization results in 826 edges and 519 triangular patches. To investigate the accuracy of the proposed method in such a mesh, we consider that the most convincing comparison is the comparison with an analytical solution. Although the structure is irregular, we can use it to study a free-space wave propagation problem whose analytical solution is known. To do so, we impose an analytical boundary condition, i.e., the known value of tangential $\mathbf{E}$, on the boundary of the problem, which comprises the innermost and outermost circles; we then numerically simulate the fields inside the computational domain and correlate the results with the analytical solution.

The incident $\mathbf{E}$, which is also the total field in the given problem, is specified as $\mathbf{E} = \hat{y} f(t - x/c)$, where $f(t) = 2(t - t_0)\exp(-(t - t_0)^2/\tau^2)$, $\tau = 2.5 \times 10^{-8}$ s, $t_0 = 4\tau$, and c denotes the speed of light. The time step used in the

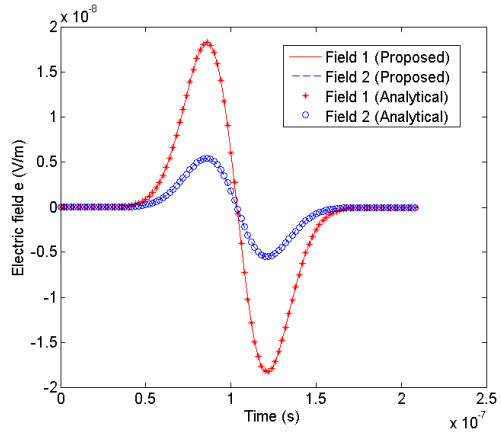

Fig. 6. Two electric fields of the ring mesh simulated from the proposed method in comparison with analytical results.

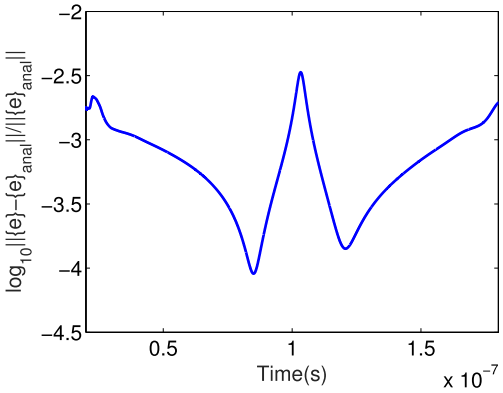

Fig. 7. $\log_{10}$ of the entire solution error for all **E** unknowns versus time.

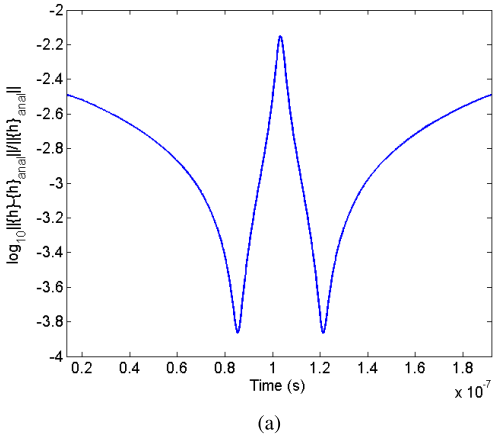

(a)

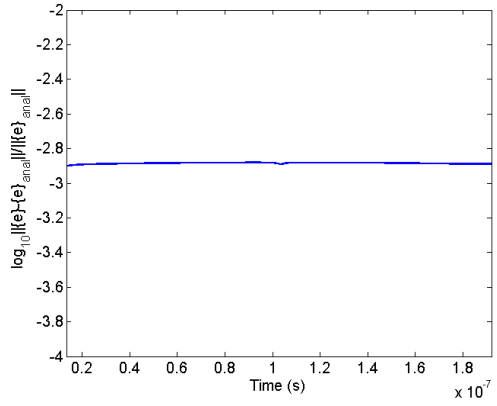

(b)

Fig. 8. (a) $\log_{10}$ of the entire solution error versus time of all **H** unknowns obtained from $\mathbf{S}_e$-rows of equations. (b) $\log_{10}$ of the entire solution error versus time of all **E** unknowns obtained from $\mathbf{S}_h$-rows of equations.

proposed method is $\Delta t = 2.0 \times 10^{-11}$ s, which is the same as what a traditional central-difference-based TDFEM has to use for stability. With this time step, the spectral radius of $\Delta t^2\mathbf{S}$ is 0.7359, and the number of expansion terms is 9 in (37). In Fig. 6, we plot the 2689th and 2690th entry randomly selected from the unknown $\{e\}$ vector, which represent $\mathbf{E}(\mathbf{r}_{ei}) \cdot \hat{e}_i$, with $i = 2689$ and 2690, respectively. The point $\mathbf{r}_{ei}$ for both i is (1.0789 m, 0.3497 m), thus the two **E** fields are sampled at the center point of one patch. From Fig. 6, it can be seen clearly that the electric fields solved from the proposed method have an excellent agreement with analytical results.

To further verify the accuracy of the proposed method, we consider the relative error of the whole solution vector defined by

$$\text{Error}_{\text{entire}}(t) = \frac{||\{e\}_{\text{this}}(t) - \{e\}_{\text{ref}}(t)||}{||\{e\}_{\text{ref}}(t)||} \tag{39}$$

as a function of time, where $\{e\}_{\text{this}}(t)$ denotes the entire unknown vector $\{e\}$ of length N_e solved from this method, while $\{e\}_{\text{ref}}(t)$ denotes the reference solution, which is analytical result $\{e\}_{\text{anal}}(t)$ in this example. Equation (39) allows us to evaluate the accuracy of the proposed method at *all* points for *all* time instants. In Fig. 7, we plot $\text{Error}_{\text{entire}}(t)$ across the whole time window in which the fields are not zero. Notice that the vertical axis displays the error in $\log_{10}$ scale, i.e., $\log_{10}\text{Error}_{\text{entire}}(t)$. It is evident that less than 1% error is observed in the entire time window, demonstrating the accuracy of the proposed method. The center peak in Fig. 7 is due to the comparison with close to zero fields.

In addition to the accuracy of the entire method, we have also examined the accuracy of the individual $\mathbf{S}_e$, and $\mathbf{S}_h$ separately, since each is important to ensure the accuracy of the whole scheme. First, to solely assess the accuracy of $\mathbf{S}_e$, we perform the time marching of (5) only without (9) by providing an analytical $\{e\}$ to (5) at each time step. The resultant $\{h\}$ is then compared to analytical $\{h\}_{\text{anal}}$ at each time step. As can be seen from Fig. 8(a) where the following **H**-error:

$$\log_{10} \frac{||h(t) - h_{\text{anal}}(t)||}{||h_{\text{anal}}(t)||} \tag{40}$$

is plotted with respect to time, the error of all **H** unknowns is less than 1% across the whole time window, verifying the accuracy of $\mathbf{S}_e$.

Similarly, in order to examine the accuracy of $\mathbf{S}_h$, we perform the time marching of (9) only without (5) by providing an analytical $\{h\}$ to (9) at each time step. The relative error of all **E** unknowns shown in (39) compared to analytical solutions in $\log_{10}$ scale is plotted with time in Fig. 8(b). Again, less than 1% error is observed across the whole time window, verifying the accuracy of $\mathbf{S}_h$.

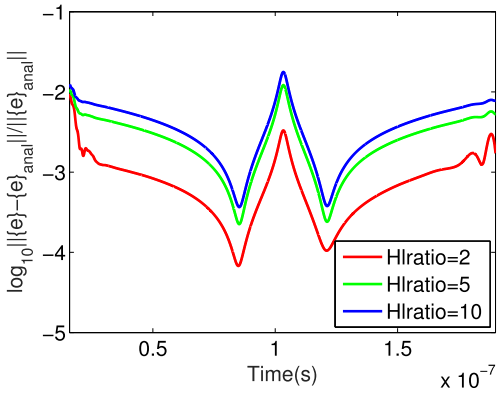

Fig. 9. $\log_{10}$ of the entire solution error for all $\mathbf{E}$ unknowns versus time.

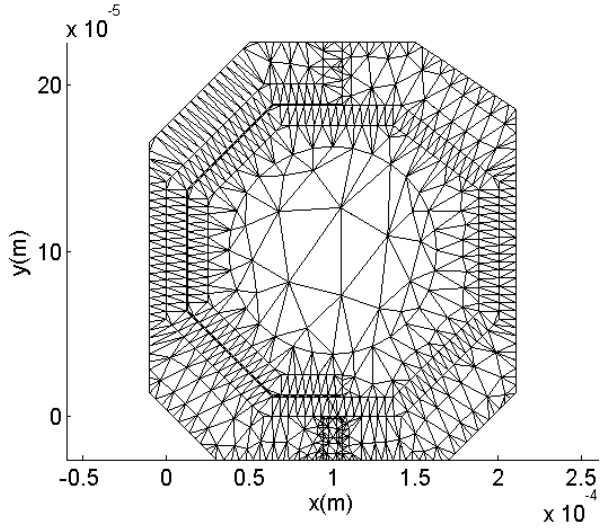

Fig. 10. Illustration of the mesh of an octagonal spiral inductor.

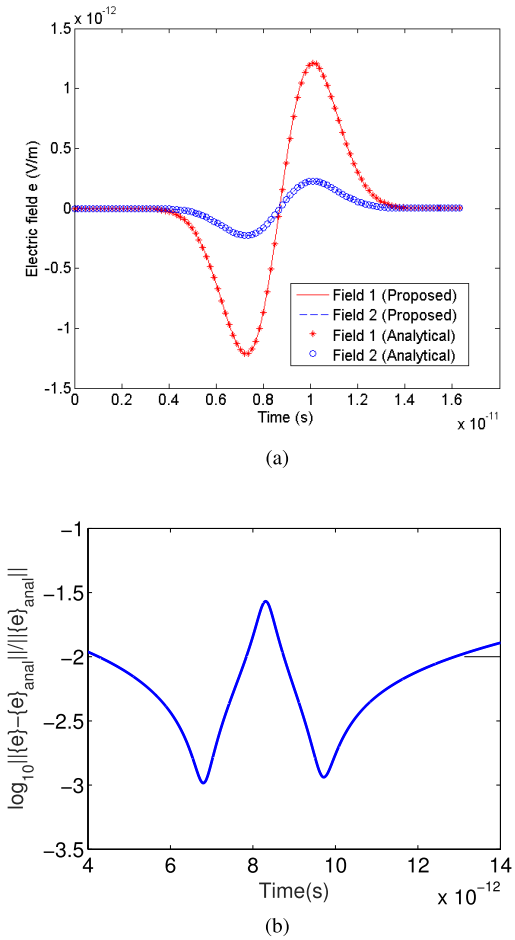

Fig. 11. Simulation of an octagonal spiral inductor mesh in comparison with analytical results. (a) Simulated two electric field waveforms. (b) $\log_{10}$ of the entire solution error versus time for all electric fields.

In this example, we have also varied the spacing between $\mathbf{H}$ points to examine its impact on time step and solution accuracy. Assume the ith vector basis at point $\mathbf{r}_{ei}$ is shared by two elements $e1$ and $e2$. We draw a line passing $\mathbf{r}_{ei}$ and perpendicular to the edge where the vector basis resides. Assume the line intersects element $e1$ at point $\mathbf{r}_1$, and $e2$ at point $\mathbf{r}_2$. If $|\mathbf{r}_1 - \mathbf{r}_{ei}| < |\mathbf{r}_2 - \mathbf{r}_{ei}|$, then the distance between the two $\mathbf{H}$ points is set to be $(2|\mathbf{r}_1 - \mathbf{r}_{ei}|)$/Hlratio. With this definition, the smaller Hlratio, the larger the distance between the two $\mathbf{H}$ points, and the smallest Hlratio one can choose is 1 for both points to fall inside the $e1$ and $e2$. As can be seen from Fig. 9, the solution accuracy is good irrespective of the choice of spacing, but larger spacing results in even better accuracy. This can be attributed to a less skewed discretization. The time step allowed by an explicit marching is 2.0×10^{-11}, 1.5×10^{-11}, and 10^{-11} s, respectively, for Hlratio $= 2,\ 5$, and 10. Hence, in general, a larger spacing is better for choice.

B. Wave Propagation in an Octagonal Spiral Inductor Mesh

The second example is a 1.5-turn octagonal spiral inductor in free space, whose 2-D mesh is shown in Fig. 10. The discretization results in 2081 edges and 1325 triangular patches. Again, we set up a free-space wave propagation problem in the given mesh to validate the accuracy of the proposed method against analytical results. The incident $\mathbf{E}$ has the same form as that of the first example, but with $\tau = 2.0 \times 10^{-12}$ s in accordance with the new structure's dimension. The outermost boundary of the mesh is truncated by analytical $\mathbf{E}$ fields. The time step used is $\Delta t = 2.0 \times 10^{-16}$ s for simulating this μm-level structure, which is the same as that used in a traditional TDFEM method. This time step results in the spectral radius of $\Delta t^2 \mathbf{S} = 0.8930$. The number of expansion terms is 9 in (37). The two degrees of freedom of the electric field located at one patch's center point (206.83 μm, 12.65 μm) are plotted in Fig. 11(a) in comparison with analytical data. Excellent agreement can be observed.

In Fig. 11(b), we plot the entire solution error shown in (39) versus time, where the vertical axis displays the error in $\log_{10}$ scale. Less than 3% error is observed in the entire time window. It is evident that the proposed method is not just accurate at certain points, but accurate at all points in the computational domain for all time instants simulated. Note that the center peak error is due to zero passing, thus the comparison with close to zero fields at the specific time instant. The actual behavior at the zero-passing time instant is more objectively reflected in Fig. 11(a). In addition, we

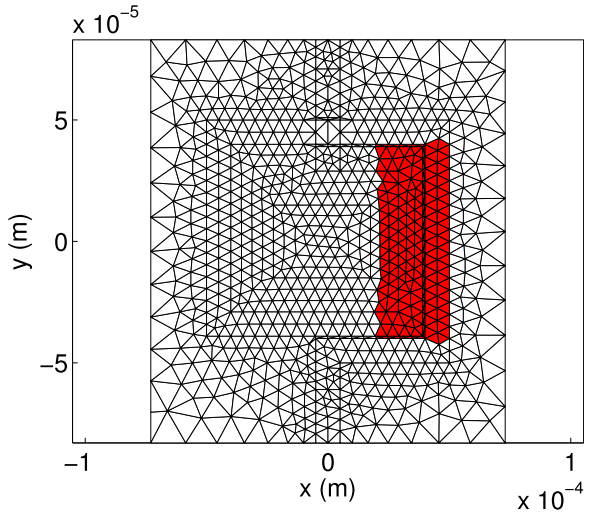

Fig. 12. Illustration of the mesh of a square inductor.

have examined the impact of k on solution accuracy. We have enlarged k from 9 to 18 and 36, the solution accuracy has no visible difference.

C. Wave Propagation and Reflection in an Inhomogeneous Medium

The third example is a wave propagation and reflection problem in an inductor mesh with dielectric materials. Fig. 12 displays the mesh details, where $\epsilon_r = 4$ in the red shaded region and 1 elsewhere. The top, bottom, and right boundaries are terminated by perfect conductors, while the left boundary is truncated by the sum of the incident and reflected $\mathbf{E}$ fields. The incident $\mathbf{E}$ has the same form as that in the first example, but with $\tau = 8.0 \times 10^{-13}$ s. The Δt used is 5.0×10^{-16} s, and the spectral radius of $\Delta t^2\mathbf{S}$ is 0.8119. The number of expansion terms is 9. In Fig. 13(a), the electric fields at two points $(-59.12, -71.31, 0)$ μm and $(-63.25, -64.3, 0)$ μm are plotted in comparison with TDFEM results. Excellent agreement can be observed. Again, such an agreement is also observed at all points for all time. As shown in Fig. 13(b), the entire solution error compared with the TDFEM solution is less than 3% at all time instants even though the mesh is highly skewed. A few peak errors are due to the comparison with close-to-zero fields.

D. Simulation of a PEC Cavity

The fourth example is a 2-D cavity. The cavity is filled with air and terminated by PEC on four sides. The mesh is shown in Fig. 14. We solve the transverse magnetic fields of TM11 mode for this cavity. The Δt used is 2.0×10^{-11} s. Nine terms are kept in (38). The same problem is also simulated using TDFEM for comparison. In Fig. 15(a), the magnetic field waveform at a randomly selected point $(0.2415, -0.0145)$ m is plotted in comparison with analytical results. Excellent agreement can be observed. Meanwhile, we calculate the entire solution error, which measures the error of the entire set of field unknowns, compared with the analytical solution at each time step for both the proposed method and the TDFEM. The errors of the two methods are shown in Fig. 15(b) as

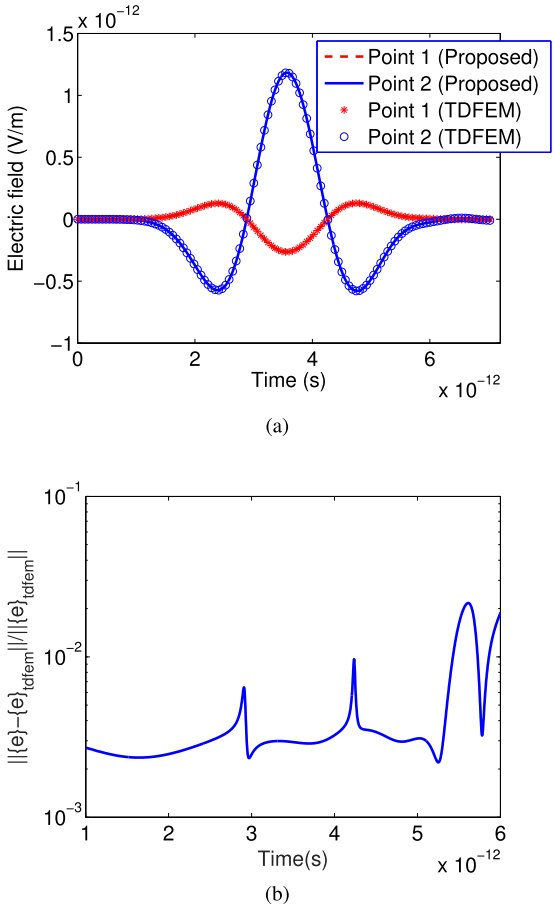

Fig. 13. (a) Electric fields at two points of a square inductor mesh simulated from the proposed method in comparison with TDFEM results. (b) Entire solution error including all electric fields versus time compared to reference TDFEM results.

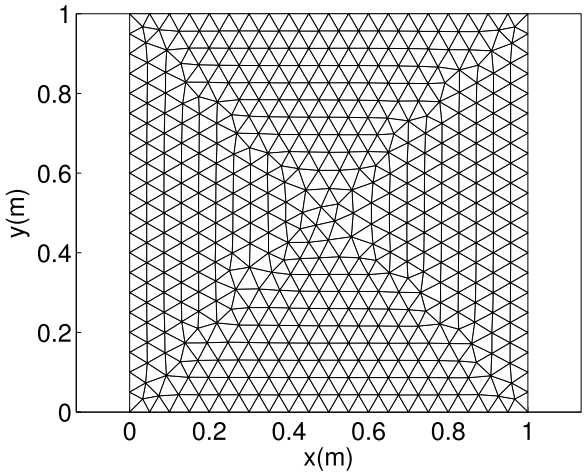

Fig. 14. Illustration of the mesh of a cavity.

a function of time. Obviously, both methods are accurate, and the proposed method is shown to have a better accuracy. This can be attributed to the better space discretization accuracy of the proposed method for the same mesh.

E. Dependence of Error on Time Step Size

To analyze how the error depends on the time step size, we simulate a wave propagation problem in a 2-D circle, whose

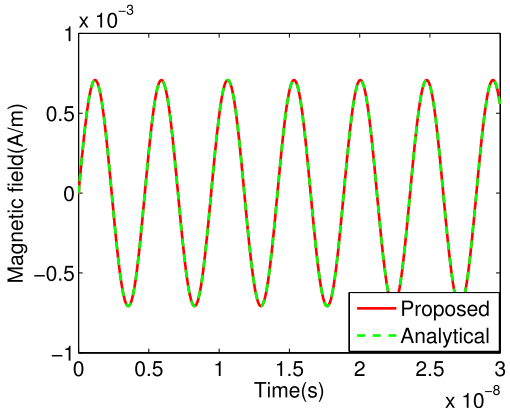

(a)

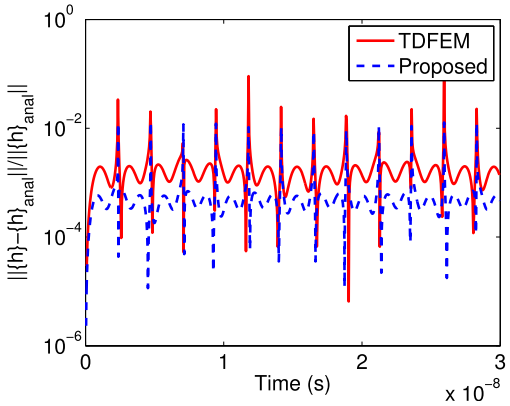

(b)

Fig. 15. (a) Magnetic field of TM11 mode at a point for a cavity simulated from the proposed method in comparison with analytical results. (b) Entire solution errors for all magnetic fields of the proposed method and the TDFEM versus time compared to analytical results.

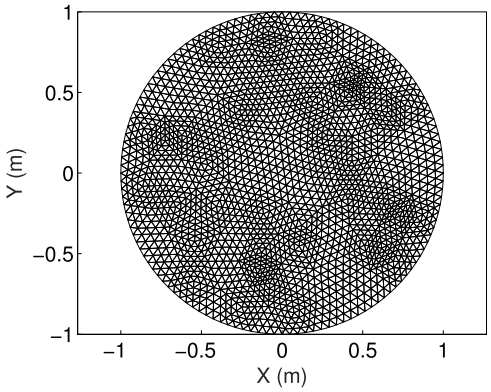

(a)

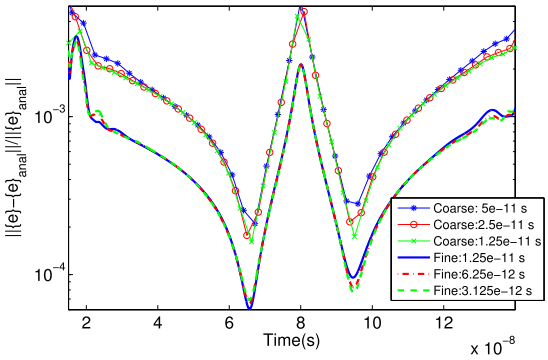

(b)

Fig. 16. (a) Illustration of the fine mesh of a circle. (b) Entire solution error versus time compared to reference analytical results with the choice of different time steps for two meshes.

mesh is shown in Fig. 16(a). The incident **E** field has the same form as is shown in Section IV-A, but with $\tau = 2.0 \times 10^{-8}$ s. An explicit marching is stable for a time step no greater than 1.25×10^{-11} s. Therefore, we choose the time step to be 1.25×10^{-11} s, 6.25×10^{-12} s, and 3.125×10^{-12} s, respectively, to run the simulation. In Fig. 16(b), the entire solution error compared with analytical solution is plotted for different time step sizes. Obviously, the proposed method can produce accurate results for all three choices of time step. As the time step decreases, there is no significant improvement in accuracy since the time step allowed by a stable explicit marching is also the one required by accuracy in the given mesh. However, the accuracy is improved more at time instants where the field solution has a more rapid temporal variation. This can be seen more clearly from the results generated from a coarser mesh, which are also plotted in Fig. 16(b).

F. Eigensolution of a Cavity Discretized Into a Highly Unstructured Mesh

The previous examples are simulated for a certain excitation. One may be interested to know the accuracy for other excitations. Furthermore, the previous examples are all simulated in time domain. How about the accuracy in frequency domain? All these questions can be addressed by finding the eigenvalue solution of **S**. This is because the field solution at any time and any frequency is a superposition of the eigenvectors of **S**, and the weight of each eigenvector can be determined from the corresponding eigenvalue. As a result, the correctness of the time-domain or frequency-domain results of the proposed method for any excitation can be found out by checking the eigensolution of **S**. We thus simulate a cavity whose analytical eigenvalues are known. The cavity is discretized into a highly irregular mesh as shown in Fig. 17 to examine the robustness of the proposed method in handling unstructured meshes. The mesh is provided by a semiconductor industry company from discretizing a real product. It appears to be of very poor quality because of accommodating all spatial features of the product, but is still a correct mesh.

We first construct matrices $\mathbf{S}_h$ and $\mathbf{S}_e$ separately, and then compute **S** based on (14), which is still a sparse matrix. We then find the eigensolution of **S** and compare the computed eigenvalues with analytical ones. The analytical eigenvalues can be found from the resonance frequencies of the cavity ω_r based on $\lambda = \omega_r^2$. In Table I, the smallest ten eigenvalues obtained from the proposed method are compared with analytical results in a descending order. It is clear that the proposed method successfully generates accurate resonance frequencies despite the poor quality of the mesh. This example also serves as a good example to show that choosing $\mathbf{S}_h = \mathbf{S}_e^T$

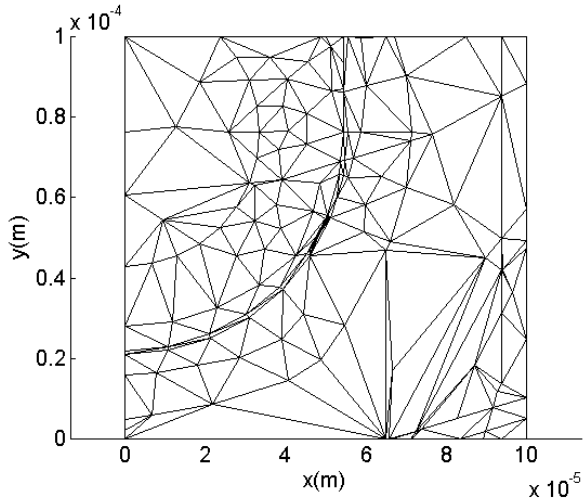

Fig. 17. Illustration of a highly irregular mesh.

TABLE I
COMPARISON OF THE SMALLEST TEN EIGENVALUES OF A CAVITY HAVING A HIGHLY IRREGULAR MESH

Analytical	This Method	Error (This)	$\mathbf{S}_h = \mathbf{S}_e^T$	Error
1.510e+27	1.451e+27	3.901e-02	1.064e+27	2.951e-01
1.421e+27	1.435e+27	9.909e-03	9.547e+26	3.282e-01
1.155e+27	1.178e+27	1.995e-02	7.516e+26	3.491e-01
8.883e+26	8.218e+26	7.482e-02	6.853e+26	2.285e-01
7.994e+26	8.180e+26	2.320e-02	6.134e+26	2.327e-01
7.106e+26	7.280e+26	2.454e-02	5.189e+26	2.697e-01
4.441e+26	4.372e+26	1.557e-02	3.296e+26	2.578e-01
3.553e+26	3.530e+26	6.457e-03	2.099e+26	4.090e-01
1.777e+26	1.806e+26	1.635e-02	9.152e+25	4.848e-01
8.883e+25	8.971e+25	9.913e-03	3.830e+25	5.688e-01

would fail to produce accuracy in such an unstructured mesh, although the accuracy at some points for some excitations can be acceptable [32]. In the fourth and fifth column of Table I, we list the eigenvalues computed by choosing $\mathbf{S}_h = \mathbf{S}_e^T$ and their relative errors compared to analytical data. Comparing the last column with the third column, the effectiveness of the proposed method is obvious in obtaining good accuracy.

V. CONCLUSION

In this paper, a new time-domain method having a naturally diagonal mass matrix is developed for solving Maxwell's equations. It is independent of element shape, thus suitable for analyzing arbitrarily shaped structures and materials discretized into unstructured meshes. The naturally diagonal mass matrix results in a strict linear computational complexity at each time step just like the complexity of an explicit FDTD method. Numerical experiments on various unstructured discretizations have validated the accuracy, stability, and generality of the proposed method. This paper has been successfully extended to 3-D analyses [24]–[27]. It is also worth mentioning that the proposed method flexibly supports higher order accuracy in both electric and magnetic fields. This can be achieved by using vector bases of any high order in each element to expand one field unknown, which consequently permits a higher order discretization of the curl of the other field unknown in the loop area normal to the first field unknown.

REFERENCES

[1] K. Yee, "Numerical solution of initial boundary value problems involving Maxwell's equations in isotropic media," *IEEE Trans. Antennas Propag.*, vol. 14, no. 3, pp. 302–307, May 1966.

[2] A. Taflove and S. C. Hagness, *Computational electrodynamics: The finite-difference time-domain method*, 3rd ed. Norwood, MA, USA: Artech House, 2000.

[3] R. Holland, "Finite-difference solution of Maxwell's equations in generalized nonorthogonal coordinates," *IEEE Trans. Nucl. Sci.*, vol. 30, no. 6, pp. 4589–4591, Dec. 1983.

[4] M. Fusco, "FDTD algorithm in curvilinear coordinates [EM scattering]," *IEEE Trans. Antennas Propag.*, vol. 38, no. 1, pp. 76–89, Jan. 1990.

[5] J.-F. Lee, R. Palandech, and R. Mittra, "Modeling three-dimensional discontinuities in waveguides using nonorthogonal FDTD algorithm," *IEEE Trans. Microw. Theory Techn.*, vol. 40, no. 2, pp. 346–352, Feb. 1992.

[6] T. G. Jurgens and A. Taflove, "Three-dimensional contour FDTD modeling of scattering from single and multiple bodies," *IEEE Trans. Antennas Propag.*, vol. 41, no. 12, pp. 1703–1708, Dec. 1993.

[7] C. H. Chan, J. T. Elson, and H. Sangani, "An explicit finite-difference time-domain method using Whitney elements," in *Proc. IEEE Int. Symp. Antennas Propag. (AP-S)*, vol. 3. Jun. 1994, pp. 1768–1771.

[8] M. Madsen, "Divergence preserving discrete surface integral methods for Maxwell's curl equations using non-orthogonal unstructured grids," *J. Comput. Phys.*, vol. 119, pp. 34–45, Sep. 1995.

[9] S. Dey and R. Mittra, "A locally conformal finite-difference time-domain (FDTD) algorithm for modeling three-dimensional perfectly conducting objects," *IEEE Microw. Guided Wave Lett.*, vol. 7, no. 9, pp. 273–275, Sep. 1997.

[10] Y. Hao and C. J. Railton, "Analyzing electromagnetic structures with curved boundaries on Cartesian FDTD meshes," *IEEE Trans. Microw. Theory Techn.*, vol. 46, no. 1, pp. 82–88, Jan. 1998.

[11] M. Cinalli and A. Schiavoni, "A stable and consistent generalization of the FDTD technique to nonorthogonal unstructured grids," *IEEE Trans. Antennas Propag.*, vol. 54, no. 5, pp. 1503–1512, May 2006.

[12] S. Gedney, F. S. Lansing, and D. L. Rascoe, "Full wave analysis of microwave monolithic circuit devices using a generalized Yee-algorithm based on an unstructured grid," *IEEE Trans. Microw. Theory Techn.*, vol. 44, no. 8, pp. 1393–1400, Aug. 1996.

[13] A. Bossavit and L. Kettunen, "Yee-like schemes on a tetrahedral mesh, with diagonal lumping," *Int. J. Numer. Model.-Electron. Netw. Devices Fields*, vol. 12, no. 1, pp. 129–142, 1999.

[14] C. F. Lee, B. J. McCartin, R. T. Shin, and J. A. Kong, "A triangular-grid finite-difference time-domain method for electromagnetic scattering problems," *J. Electromagn. Waves Appl.*, vol. 8, no. 4, pp. 449–470, 1994.

[15] M. Hano and T. Itoh, "Three-dimensional time-domain method for solving Maxwell's equations based on circumcenters of elements," *IEEE Trans. Magn.*, vol. 32, no. 3, pp. 946–949, May 1996.

[16] S. D. Gedney and J. A. Roden, "Numerical stability of nonorthogonal FDTD methods," *IEEE Trans. Antennas Propag.*, vol. 48, no. 2, pp. 231–239, Feb. 2000.

[17] D. Jiao and J. Jin, "The finite element method in electromagnetics," in *Finite Element Analysis in Time Domain*. Hoboken, NJ, USA: Wiley, 2002, pp. 529–584.

[18] M.-F. Wong, O. Picon, and V. F. Hanna, "A finite element method based on Whitney forms to solve Maxwell equations in the time domain," *IEEE Trans. Magn.*, vol. 31, no. 3, pp. 1618–1621, May 1995.

[19] M. Feliziani and F. Maradei, "Hybrid finite element solutions of time dependent Maxwell's curl equations," *IEEE Trans. Magn.*, vol. 31, no. 3, pp. 1330–1335, May 1995.

[20] D. A. White, "Orthogonal vector basis functions for time domain finite element solution of the vector wave equation [EM field analysis]," *IEEE Trans. Magn.*, vol. 35, no. 3, pp. 1458–1461, Mar. 1999.

[21] D. Jiao and J.-M. Jin, "Three-dimensional orthogonal vector basis functions for time-domain finite element solution of vector wave equations," *IEEE Trans. Antennas Propag.*, vol. 51, no. 1, pp. 59–66, Jan. 2003.

[22] S. D. Gedney *et al.*, "The discontinuous Galerkin finite element time domain method (DGFETD)," in *Proc. IEEE Int. Symp. Antennas Propag.*, Aug. 2008, pp. 1–4.

[23] S. D. Gedney, J. C. Young, T. C. Kramer, and J. A. Roden, "A discontinuous Galerkin finite element time-domain method modeling of dispersive media," *IEEE Trans. Antennas Propag.*, vol. 60, no. 4, pp. 1969–1977, Apr. 2012.
[24] J. Yan and D. Jiao, "Accurate matrix-free time-domain method in three-dimensional unstructured meshes," in *Proc. IEEE Int. Symp. Antennas Propag.*, Jul. 2015, pp. 1830–1831.
[25] J. Yan and D. Jiao, "Accurate matrix-free time-domain method with traditional vector bases in unstructured meshes," in *Proc. IEEE Int. Symp. Antennas Propag.*, Jul. 2015, pp. 342–343.
[26] J. Yan and D. Jiao, "Accurate and stable matrix-free time-domain method in 3-D unstructured meshes for general electromagnetic analysis," *IEEE Trans. Microw. Theory Techn.*, vol. 63, no. 12, pp. 4201–4214, Sep. 2015.
[27] J. Yan and D. Jiao, "Matrix-free time-domain method for general electromagnetic analysis in 3-D unstructured meshes—Modified-basis formulation," *IEEE Trans. Microw. Theory Techn.*, vol. 64, no. 8, pp. 2371–2382, Oct. 2016.
[28] R. D. Graglia, D. R. Wilton, and A. F. Peterson, "Higher order interpolatory vector bases for computational electromagnetics," *IEEE Trans. Antennas Propag.*, vol. 45, no. 3, pp. 329–342, Mar. 1997.
[29] Q. He, H. Gan, and D. Jiao, "Explicit time-domain finite-element method stabilized for an arbitrarily large time step," *IEEE Trans. Antennas Propag.*, vol. 60, no. 11, pp. 5240–5250, Nov. 2012.
[30] F. Tisseur and K. Meerbergen, "The quadratic eigenvalue problem," *SIAM Rev.*, vol. 43, no. 2, pp. 235–286, 2001.
[31] P.-O. Persson and G. Strang, "A simple mesh generator in MATLAB," *SIAM Rev.*, vol. 46, no. 2, pp. 329–345, 2004.
[32] J. Yan and D. Jiao, "A matrix-free time-domain method independent of element shape for electromagnetic analysis," in *Proc. IEEE Int. Symp. Antennas Propag. (AP-S)*, Sep. 2014, pp. 2258–2259.

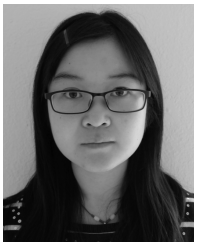

Jin Yan (S'13) received the B.S. degree in electronic engineering and information science from the University of Science and Technology of China, Hefei, China, in 2012. She is currently pursuing the Ph.D. degree in electrical engineering with Purdue University, West Lafayette, IN, USA.

She is currently with the On-Chip Electromagnetics Group, Purdue University. Her current research interests include computational electromagnetics, high-performance very large scale integration CAD, and fast and high-capacity numerical methods.

Ms. Yan was a recipient of an Honorable Mention Award of the IEEE International Symposium on Antennas and Propagation in 2015, and the Best Student Paper Award Finalist from the IEEE International Microwave Symposium in 2016.

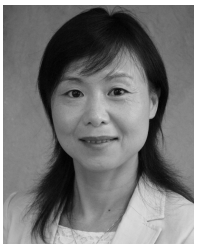

Dan Jiao (M'02–SM'06–F'16) received the Ph.D. degree in electrical engineering from the University of Illinois at Urbana–Champaign, IL, USA, in 2001.

She was with the Technology Computer-Aided Design (CAD) Division, Intel Corporation, Santa Clara, CA, USA, until 2005, as a Senior CAD Engineer, a Staff Engineer, and a Senior Staff Engineer. In 2005, she joined Purdue University, West Lafayette, IN, USA, as an Assistant Professor with the School of Electrical and Computer Engineering, where she is currently a Professor. She has authored three book chapters and over 240 papers in refereed journals and international conferences. Her current research interests include computational electromagnetics, high-frequency digital, analog, mixed-signal, RF integrated circuit design and analysis, high-performance very large scale integration CAD, modeling of microscale and nanoscale circuits, applied electromagnetics, fast and high-capacity numerical methods, fast time-domain analysis, scattering and antenna analysis, RF, microwave, millimeter-wave circuits, wireless communication, and bioelectromagnetics.

Dr. Jiao was a recipient of the 2010 Ruth and Joel Spira Outstanding Teaching Award, the 2008 National Science Foundation CAREER Award, the 2006 Jack and Cathie Kozik Faculty Start up Award (which recognizes an outstanding new faculty member of the School of Electrical and Computer Engineering, Purdue University), the 2006 Office of Naval Research Award under the Young Investigator Program, the 2004 Best Paper Award presented at the Intel Corporation annual corporate-wide technology conference (Design and Test Technology Conference) for her work on generic broadband model of high-speed circuits, the 2003 Intel Corporation Logic Technology Development (LTD) Divisional Achievement Award, the Intel Corporation Technology CAD Divisional Achievement Award, the 2002 Intel Corporation Components Research the Intel Hero Award (Intel-wide she was the tenth recipient), the Intel Corporation LTD Team Quality Award, and the 2000 Raj Mittra Outstanding Research Award presented by the University of Illinois at Urbana–Champaign. She was also a recipient of the 2013 S. A. Schelkunoff Prize Paper Award of the IEEE Antennas and Propagation Society, which recognizes the Best Paper published in the IEEE TRANSACTIONS ON ANTENNAS AND PROPAGATION during the previous year. She has served as the reviewer for many IEEE journals and conferences. She is an Associate Editor of the IEEE TRANSACTIONS ON COMPONENTS, PACKAGING, AND MANUFACTURING TECHNOLOGY. She was among the 21 women faculty selected across the country as the 2014–2015 Fellow of Executive Leadership in Academic Technology and Engineering at Drexel, a national leadership program for women in the academic STEM fields. She has been named a University Faculty Scholar by Purdue University since 2013. She was among the 85 engineers selected throughout the nation for the National Academy of Engineering 2011 U.S. Frontiers of Engineering Symposium.